

Published in final edited form as:

*IEEE Trans Med Imaging*. 2008 May ; 27(5): 664–673. doi:10.1109/TMI.2007.913279.

## Hamilton-Jacobi Skeleton on Cortical Surfaces

Yonggang Shi [Member, IEEE], Paul M. Thompson, Ivo Dinov, and Arthur W. Toga\*  
[Member, IEEE]

Department of Neurology, Laboratory of Neuro Imaging, UCLA School of Medicine, Los Angeles, CA 90095, USA

### Abstract

In this paper, we propose a new method to construct graphical representations of cortical folding patterns by computing skeletons *on* triangulated cortical surfaces. In our approach, a cortical surface is first partitioned into sulcal and gyral regions via the solution of a variational problem using graph cuts, which can guarantee global optimality. After that, we extend the method of Hamilton-Jacobi skeleton [1] to subsets of triangulated surfaces, together with a geometrically intuitive pruning process that can trade off between skeleton complexity and the completeness of representing folding patterns. Compared with previous work that uses skeletons of 3D volumes to represent sulcal patterns, the skeletons on cortical surfaces can be easily decomposed into branches and provide a simpler way to construct graphical representations of cortical morphometry. In our experiments, we demonstrate our method on two different cortical surface models, its ability of capturing major sulcal patterns and its application to compute skeletons of gyral regions.

### Keywords

Cortex; folding pattern; graphical representation; skeleton; triangular mesh

## I. Introduction

One key problem in brain mapping is to study the relation between cortical morphometry and brain functions [2]-[5]. With 3D MRI technologies, it is now possible to obtain structural information of the brain from a large population *in vivo*. In order to test various hypotheses on cortical morphometry to functions, genetics, and pathologies, it is necessary that we first build mathematical representations of cortical folding patterns. To this end, we propose in this paper, a new method to construct graphical representations of the sulcal and gyral regions by extending the method of Hamilton-Jacobi skeleton [1] to triangulated cortical surfaces.

Skeletons, or medial models, are important tools in studying shapes [1], [6]-[8]. The skeleton of subsets in *volume* images was used to represent sulcal patterns in previous works. The medial model of the union of the gray matter and cerebrospinal fluid (CSF) was computed to represent the sulcal regions [9], which was further decomposed into simple surfaces, or sulcal ribbons, based on the digital topology of 3D grids such that a graphical model can be constructed with these simple surfaces as the graph nodes. The work in [10] also used digital topology in 3D volumes to detect sulcal and gyral lines. A graphical

structure of the sulcal regions was computed in [11] on the exterior hull of the cortex by applying a thinning process to the sulcal regions. Each branch of the graph was further used to construct sulcal ribbons [12]-[14] with an active contour evolution. This graphical structure can be used to analyze cortical morphometry and help semi-automatically [11] or automatically label the major sulci [15].

With the advance of cortical segmentation techniques, surface-based approaches have become increasingly popular in brain mapping studies [16]-[18] because their ability of capturing the intrinsic geometry of the cortex. In this work, we propose a skeleton-based method to extract graphical representations of cortical folding patterns from the *surface* representation of a cortex. As illustrated in Fig. 1, there are two main steps in our method. In the first step, we develop a graph-cut method to partition the cortical surface into sulcal and gyral regions. In the second step, the method of Hamilton-Jacobi skeleton is extended to subsets of triangular meshes to compute a homotopic skeleton for the sulcal or gyral regions. We use the triangular mesh representation for cortical surfaces as this is the output format of many popular cortical surface extraction algorithms [19]-[26]. One advantage of working on the triangular mesh is that there is no ambiguity in the 2D neighboring relation for vertices on the mesh, thus the digital topology over triangulated surfaces is much simpler than that of 3D grids, where multiple choices exist in defining neighboring relations [27], [28]. As a result, it is straightforward to decompose the skeleton into branches on triangular cortical surfaces and use them to construct graphical representations of cortical morphometry.

Among all the sulcal lines, a set of major sulci that are stable across populations provide boundary conditions in computing maps between cortices [17], [18], [29], [30]. Various approaches have been proposed to detect these major sulci on cortical surfaces [31]-[36]. By constructing a graphical representation from the skeleton of the sulcal or gyral regions, our algorithm transforms the folding pattern, which is implicitly encoded in the surface geometry of the cortex, into a set of explicitly represented line segments. Using this explicit representation, semi-automatic approaches can be easily developed that require very few user interactions to pick out each major sulcus from the set of sulcal lines. By equipping the graph with probabilistic models that can be learned from training data, it is also possible to develop automated tools for sulci labeling [15].

Using a novel depth measure derived from an exterior hull of the cortex, a related work in [37] proposed to extract a network of sulcal lines from a cortical surface model by first detecting a set of end points of the sulcal regions and then connecting them with a spanning tree. However, circular paths exist frequently in the sulcal regions. Thus, the assumption of a tree structure can result in missing important branches in the line representation of the sulcal pattern, which may affect the accuracy of further analytic tasks. In this work, we use curvature features of the cortical surface to define the sulcal and gyral regions. By computing the Hamilton-Jacobi skeleton of the sulcal regions, our method can extract a network representation of the cortical folding pattern that is homotopic to the sulcal regions. The skeleton extraction approach we develop here is also applicable to general regions on triangulated surfaces, for example the gyri.

In the rest of the paper, we first present in section II our graph-cut method for the segmentation of sulcal and gyral regions. After that, the Hamilton-Jacobi skeleton is extended to triangular meshes in section III, together with a pruning method that provides a geometrically intuitive stopping criterion. Experimental results are presented in section IV. Finally, conclusions are made in V.

## II. Graph-cut segmentation

In this section, we develop a variational approach to segment a cortical surface into sulcal and gyral regions. We assume the cortical surface is represented as a triangular mesh  $\mathcal{M} = (\mathcal{V}, \mathcal{T})$ , where  $\mathcal{V} = \{\mathcal{V}_i\}_{i=1}^K$  and  $\mathcal{T} = \{\mathcal{T}_i\}_{i=1}^L$  are the set of vertices and triangles in the mesh. Our goal is to classify all vertices into two sets  $R_s$  and  $R_g$  which represent the sulcal and gyral regions, respectively.

For the segmentation of the surface  $\mathcal{M}$ , we define a feature function at each vertex  $f: \mathcal{V}_i \rightarrow \mathbb{R}$  with the aim of differentiating the sulcal from gyral regions. Both curvature [31], [32], [35] and depth features [37], [38] were used in previous works on sulci detection. In this work, we use the mean curvature as the feature function  $f$  because it is easy to compute and very effective in summarizing the geometric characteristics of the cortical surface. Nevertheless the graph-cut approach we develop here can be easily adapted to other feature functions. For the numerical evaluation of the mean curvature, we use existing modules in LONI Pipeline [39] that first converts a triangulated cortical surface into a signed distance function and then computes the mean curvature using the level-set method [40].

As illustrated in Fig. 2(a) and (b), the mean curvature is typically negative in the sulcal regions and positive in the gyral regions. However, simple thresholding may result in a very noisy segmentation as shown in Fig. 2(c) and (d). To incorporate regularization into the segmentation, we compute it as the minimizer of a variational problem with the energy defined as:

$$E(R_s, R_g) = - \sum_{\mathcal{V}_i \in R_s} \log p_s(f(\mathcal{V}_i)) - \sum_{\mathcal{V}_i \in R_g} \log p_g(f(\mathcal{V}_i)) + \lambda \sum_{i=1}^K \sum_{\mathcal{V}_j \in N(\mathcal{V}_i)} \delta(\mathcal{V}_i, \mathcal{V}_j) \quad (1)$$

The first two terms of the energy are data fidelity terms and defined as the negative log-likelihood of the feature distribution  $p_s$  and  $p_g$  in the sulcal and gyral regions, respectively, both of which are represented as Gaussian distributions. Given a cortical surface, we can estimate the mean and variance of the feature distribution  $p_s$  from the histogram of all negative features. Similarly, the parameters of  $p_g$  are estimated from the histogram of all positive features. Though it is also possible to use more sophisticated parametric forms such as Gaussian mixtures to model the feature distributions, we find in our experience the distribution of the mean curvature on a cortical surface is mostly bimodal, as illustrated in the histogram in Fig. 3. Thus the simple Gaussian models adopted here provide a fairly good balance between model complexity and robustness, and they perform very well in practice.

The third term in the energy is for regularization and penalizes discontinuities between neighboring vertices. For this purpose, geodesic smoothing was used in [41]. In our variational approach, we use the Markov random field model by incorporating an edge

indicator function  $\delta(\mathcal{V}_i, \mathcal{V}_j)$  in the energy, which is defined as one when  $\mathcal{V}_i$  and  $\mathcal{V}_j$  belong to different regions and zero otherwise. This energy term is thus only effective when a vertex  $\mathcal{V}_i$  and its neighbor  $\mathcal{V}_j$  cross the region boundary. The neighborhood  $N(\mathcal{V}_i)$  of a vertex  $\mathcal{V}_i$  is defined as its one-ring neighborhood. The regularization parameter  $\lambda$  is used to balance the weight between data fidelity and boundary smoothness.

To minimize the energy, we need to find the solution for a Markov random field problem. Conventionally techniques such as simulated annealing [42] and iterated conditional modes (ICM) [43] were used. Here we use the graph-cut method [44], [45] because it can efficiently compute the global minimum for such binary optimization problems. For this

purpose we construct a graph  $\mathcal{G} = (\bar{\mathcal{V}}, \mathcal{E})$  as follows. The set of vertices in  $\mathcal{G}$  is defined as  $\bar{\mathcal{V}} = \mathcal{V} \cup \{T_s, T_g\}$ , which is the union of vertices in the mesh  $\mathcal{M}$  and two terminal nodes  $T_s$  and  $T_g$ . The edge set  $\mathcal{E}$  in  $\mathcal{G}$  is composed of two type of edges as illustrated in Fig. 4: t-links that connect vertices in  $\mathcal{V}$  to  $T_s$  or  $T_g$ , and n-links that connect neighboring vertices in  $\mathcal{V}$ . The weight of t-links take into account the data fidelity term and are defined as  $w(\mathcal{V}_i, T_s) = -\log p_g(f(\mathcal{V}_i))$  and  $w(\mathcal{V}_i, T_g) = -\log p_s(f(\mathcal{V}_i))$ . The weight of n-links account for the regularization term and are defined as:

$$w(\mathcal{V}_i, \mathcal{V}_j) = \lambda$$

if  $\mathcal{V}_j \in N(\mathcal{V}_i)$ . To compute the graph cut, we use the max-flow algorithm in [45], which computes the maximum flow from the sulcal region terminal node to the gyral region terminal node. The final cut is obtained at those edges with saturated flows. For graphs with two terminal nodes as the one in Fig. 4, optimal solutions are guaranteed [44], [45]. From the result of the graph cut, the region  $R_s$  is obtained as the set of vertices connected to the terminal node  $T_s$ , and the region  $R_g$  as the set of vertices connected to the terminal node  $T_g$ .

As an example, the segmentation result for the cortical surface in Fig. 2 is shown in Fig. 5(a) and (b) from the lateral and medial view, where the parameter is  $\lambda = 1$ . As compared to the result in Fig. 2(c) and (d), we can see a much cleaner segmentation has been obtained with graph cuts due to the incorporation of regularization. The computational process is also very efficient and typically takes only several seconds.

### III. Hamilton-Jacobi Skeleton of Regions on Cortical Surfaces

In this section, we construct a graphical representation for the segmented sulcal or gyral regions on a cortical surface by computing their Hamilton-Jacobi skeletons. The method of Hamilton-Jacobi skeleton was originally proposed for shapes embedded in  $\mathbb{R}^2$  or  $\mathbb{R}^3$ . Using the fast marching algorithm on triangular meshes [46], we first extend it to compute the skeleton of an object region on a triangulated surface. We then construct a graphical representation of the cortical folding pattern by decomposing the skeleton into a set of branches. Based on this representation, a pruning algorithm is developed to provide a geometrically intuitive stopping criterion to generate the final skeleton and graphical representation.

#### A. Skeleton computation

Let  $\mathcal{O} \subset \mathbb{R}^2$  or  $\mathbb{R}^3$  be an object region and  $D$  be its distance transform. To compute the Hamilton-Jacobi skeleton of  $\mathcal{O}$ , the basic idea is to extract the singularities of the distance transform  $D$  with a robust measure, which is the average flux of the vector field  $\Delta D$  at each point of  $\mathcal{O}$ . The intuition is that this measure is close to zero for points away from the skeleton and has large negative magnitude on the skeleton. The averaging process also has a low pass filtering effect and thus the skeleton extracted based on the flux measure is robust to small perturbations of object boundaries. Combined with the concept of simple points and end points from digital topology, a flux-ordered and homotopy-preserving thinning algorithm was developed to robustly extract the skeleton of the object [1].

For an object region  $\mathcal{O} \subset \mathcal{V}$  on the triangular mesh  $\mathcal{M}$ , we define its boundary set as:

$$\mathcal{B}(\mathcal{O}) = \{\mathcal{V}_i \in \mathcal{O} | \exists \mathcal{V}_j \in N(\mathcal{V}_i) \text{ s.t. } \mathcal{V}_j \in \mathcal{V} \setminus \mathcal{O}\}. \quad (2)$$

Note that the object region  $\mathcal{O}$  can be composed of multiple connected components, such as the sulcal regions on a cortical surface. The region  $\mathcal{V} \setminus \mathcal{O}$  is denoted as the background region. As a first step in extracting the skeleton of the region  $\mathcal{O}$ , we compute its intrinsic distance transform  $D$  on the cortical surface  $\mathcal{M}$  by solving the following Eikonal equation

$$\|\nabla_{\mathcal{M}} D\| = 1 \quad (3)$$

given the boundary condition

$$D(\mathcal{V}_i) = 0 \quad \forall \mathcal{V}_i \in \mathcal{B}(\mathcal{O}),$$

where  $\nabla_{\mathcal{M}} D$  is the intrinsic gradient of the distance function over the manifold  $\mathcal{M}$ . For numerical implementation, we use the fast marching algorithm on triangular meshes [46] to solve Eq. (3) and obtain the distance function  $D$ .

From a front propagation point of view, the skeleton of the region  $\mathcal{O}$  is where the fronts originated from the boundary set  $\mathcal{B}(\mathcal{O})$  meet and form shocks. To detect these skeletal points, we define at each vertex  $\mathcal{V}_i$  on  $\mathcal{M}$  the average flux analogously to the flux measure in [1] as

$$\text{Flux}(\mathcal{V}_i) = \frac{\int_{\delta R} \langle \vec{N}, \nabla_{\mathcal{M}} D \rangle ds}{\int_{\delta R} ds} \quad (4)$$

where  $\delta R$  is the boundary of an infinitesimal geodesic neighborhood of  $\mathcal{V}_i$ ,  $\vec{N}$  is the outward normal direction of  $\delta R$  and  $\nabla_{\mathcal{M}} D$  is the intrinsic gradient of  $D$  on the manifold  $\mathcal{M}$ . For numerical approximation, we evaluate the flux measure at  $\mathcal{V}_i$  as

$$\text{Flux}(\mathcal{V}_i) \approx \frac{1}{n} \sum_{j=1}^n \langle \frac{\overrightarrow{\mathcal{V}_i \mathcal{V}_j}}{\|\overrightarrow{\mathcal{V}_i \mathcal{V}_j}\|}, \nabla_{\mathcal{M}} D(\mathcal{V}_j) \rangle \quad (5)$$

where  $n$  is the number of neighboring vertices in the 1-ring neighborhood of  $\mathcal{V}_i$ ,

$\mathcal{V}_j$  ( $j=1, \dots, n$ ) are vertices in this neighborhood, and  $\overrightarrow{\mathcal{V}_i \mathcal{V}_j}$  is the vector from the vertex  $\mathcal{V}_i$  to  $\mathcal{V}_j$ .

For the cortical surface shown in Fig. 5, we computed the flux measure for vertices in both the sulcal and gyral regions. From the result visualized in Fig. 6, a naive way of locating the skeleton of the sulcal or gyral regions is then sequentially removing vertices with the flux measure above certain threshold from the object boundary. To ensure the skeleton is a thin set homotopic to the object region, however, we must extend to triangular meshes the concept of *simple points* and *end points* such that a homotopy-preserving thinning process can be developed.

A point of an object region is called *simple* if its removal will not change the topology of the object region, which means no holes will be created and originally connected components will not be disconnected. A thinning process is homotopic if only simple points are removed from the object region [27], [28], [47]. The concept of simple points was extended to triangular meshes in [48] and we formalize the definition here for completeness.

**Definition 1**—A vertex in an object region of a triangular mesh is a **simple point** if its 1-ring neighborhood is composed of vertices from both the object and background region and both of them form one connected component.

To illustrate the basic idea of simple points on triangular meshes, we consider three different cases in Fig. 7 for the 1-ring neighborhood of a vertex. For the cases in Fig. 7(a) and (b), removing the vertex may either disconnect the object region or form a hole. On the contrary, both the object and background vertices in Fig. 7(c) form one connected component and thus the removal of the center vertex will not change the topology.

To ensure the final skeleton is a thin set with no interior, we also extend the notion of end points to triangular meshes with the following definition.

**Definition 2**—A vertex in an object region of a triangular mesh is an **end point** if only one vertex in its 1-ring neighborhood belongs to the object region.

During the thinning process of computing the Hamilton-Jacobi skeleton, a preselected threshold  $F_{thd}$  is only applied to end points of the region, while other points are removed sequentially according to their flux measures if they satisfy the condition of being simple points. This ensures that the final skeleton is a thin set of width one. Summarizing the above development, the extended algorithm for computing the Hamilton-Jacobi skeleton on the triangular mesh  $\mathcal{M}$  is listed in Table I.

## B. Graphical model construction

If we use the sulcal regions as the object region on the cortical surface, the output of our skeletonization algorithm is a set of vertices  $S$  on  $\mathcal{M}$  that is homotopic to the sulcal regions. To construct a graphical model from the skeleton, we first mark the set of terminal points in  $S$  as

$$TP = \{v \in S \mid \#(N(v) \cap S) = 1 \text{ or } \geq 3\} \quad (6)$$

which are skeletal points with one or at least three neighboring vertices in the set  $S$ . By breaking the skeleton at terminal points, we can decompose it into a set of branches  $\mathcal{B}$  with each member of  $\mathcal{B}$  as a connected line segment on the mesh. These branches form the nodes of our graphical model and play the same role in our model as the simple surfaces in the model used in [9], [15]. Two branches  $b_1$  and  $b_2$  are connected with each other if  $\exists v_i \in TP \cap b_1$  and  $\exists v_j \in TP \cap b_2$  such that  $v_i \in N(v_j)$ . With neighboring relation, we have a graphical model of sulcal lines to represent the folding pattern of the cortical surface.

The complexity of the graphical model constructed from the Hamilton-Jacobi skeleton is controlled by the threshold parameter  $F_{thd}$  in Table I. To illustrate the effect of this parameter, we show in Fig. 8 the skeleton of the sulcal regions shown in Fig. 5 computed by choosing the threshold as the 50th, 25th, and 5th percentile of the flux measures from all the vertices in the sulcal regions. For each branch in the skeleton, we mark its terminal points with yellow dots. With decreasing of the threshold  $F_{thd}$ , we can see more branches are eliminated, which is especially easy to see from the density of the yellow dots in the region enclosed by the blue ellipse in Fig. 8(d), (e), (f). However one problem with using the threshold  $F_{thd}$  to control the final skeleton is that its relation to the geometric properties of the skeleton is unclear. For example, we see the medial end of the central sulcus, pointed by the blue arrow in Fig. 8(a), (b), (c), is eliminated if the parameter  $F_{thd}$  is set too small. On the other hand, the branch pointed by the green arrow in Fig. 8(d), (e), (f) persists in all three cases, even though the ending part of the central sulcus identified by the blue arrow is visually more significant. To avoid this problem, we next develop a geometrically intuitive



pruning algorithm and apply it to the Hamilton-Jacobi skeleton to generate the final skeleton.

### C. Skeleton pruning

Before we start the pruning process, we classify the branches  $\mathcal{B}$  of the Hamilton-Jacobi skeleton into three types:

- Independent branch set  $\mathcal{B}_i$ : no neighbors.
- Terminal branch set  $\mathcal{B}_t$ : only one terminal point connected to neighbors.
- Middle branch set  $\mathcal{B}_m$ : both terminal points connected to neighbors.

By pruning small branches, our goal is to identify major folding patterns of cortical surfaces. In deciding the pruning order, we define a significance measure based on the geometric properties of the branch. For each branch of the skeleton in the set  $\mathcal{B}_i$  and  $\mathcal{B}_t$ , its significance measure is a combination of its length and continuity with neighboring branches [8]. For two neighboring branches  $b_1$  and  $b_2$ , we denote their terminal points as  $(\mathcal{V}_{1,1}, \mathcal{V}_{1,2})$  and  $(\mathcal{V}_{2,1}, \mathcal{V}_{2,2})$ , respectively. Since  $b_1$  and  $b_2$  are neighbors, we assume  $\mathcal{V}_{2,1} \in N(\mathcal{V}_{1,2})$  and define the continuity between them as

$$C(b_1, b_2) = \exp \left( - \left\langle \frac{\overrightarrow{\mathcal{V}_{1,2} \mathcal{V}_{1,1}}}{\|\overrightarrow{\mathcal{V}_{1,2} \mathcal{V}_{1,1}}\|}, \frac{\overrightarrow{\mathcal{V}_{2,1} \mathcal{V}_{2,2}}}{\|\overrightarrow{\mathcal{V}_{2,1} \mathcal{V}_{2,2}}\|} \right\rangle \right) \quad (7)$$

where  $\overrightarrow{\mathcal{V}_i \mathcal{V}_j}$  denotes a vector from  $\mathcal{V}_i$  to  $\mathcal{V}_j$ , and the continuity measure increases monotonically with respect to the angle between the two vectors  $\overrightarrow{\mathcal{V}_{1,2} \mathcal{V}_{1,1}}$  and  $\overrightarrow{\mathcal{V}_{2,1} \mathcal{V}_{2,2}}$ . Based on this continuity measure, we define the pruning weight for each independent and terminal branch as:

$$W(b_i) = \begin{cases} l(b_i) & \text{if } b_i \in \mathcal{B}_i \\ l(b_i) \max_{b_j \in N(b_i)} C(b_i, b_j) & \text{if } b_i \in \mathcal{B}_t \end{cases} \quad (8)$$

where  $l(b_i)$  is the length of the branch  $b_i$ , and  $N(b_i)$  denotes the set of neighboring branches of  $b_i$ .

Using this significance measure, we prune the skeleton by sequentially eliminating the branch with the lowest weight until all branches left in  $\mathcal{B}_i \cup \mathcal{B}_t$  have weights greater than a preselected threshold  $S_0$  proportional to branch length. During this pruning process, the graph structure of the skeleton also needs to be updated dynamically to take into account the changing neighboring relation, branch type, and significance measure of those branches connected to the eliminated branch. For example, if a branch in  $\mathcal{B}_m$  merges with a branch in  $\mathcal{B}_t$ , its category is updated from a member of  $\mathcal{B}_m$  to  $\mathcal{B}_t$ . But since no branches in the set is  $\mathcal{B}_m$  eliminated in any pruning operation, we still have homotopic skeletons for large connected components of the object region since the parameter  $S_0$  is typically chosen to be much smaller than the length of major sulci. By changing the parameter  $S_0$ , we can trade off between the complexity of the skeleton and its completeness in representing cortical folding patterns. As a summary, the pruning algorithm is listed in Table II.

To illustrate the effect of pruning, we show in Fig. 9 the skeleton obtained after applying the pruning algorithm with  $S_0 = 15 \text{ mm}$  to the Hamilton-Jacobi skeleton in Fig. 8(b) and (d). We can see that the pruning algorithm is able to eliminate the small branch at the medial end of

the central sulcus, which is now a single branch in the final skeleton and can be picked out easily with minimal user interaction. It is also clear that the small branch pointed by the green arrow in Fig. 8 (d) is removed successfully. This shows the pruning algorithm provides a geometrically intuitive way to control the final result of the Hamilton-Jacobi skeleton.

## IV. Experimental Results

In this section, we present experimental results to demonstrate our algorithm. Cortical surface models generated from two different methods were used in our experiments. For experiments in section IV-A, B, and C, we used surface models extracted by an algorithm that deforms a spherical mesh to the boundary between the gray matter and cerebrospinal fluid (CSF) [19]. Typical resolution of the mesh is 1mm as measured by the length of edges. Even though surface models generated with this method may not capture the deepest parts of sulcal regions, they have more regularity across population and can greatly decrease registration difficulties in group studies. Besides the brain surface between the CSF and gray matter, we applied our algorithm to two surfaces generated by BrainVISA [49] in section IV-D, which represent the boundary between the white and gray matter. For the purpose of analyzing cortical folding patterns, we have chosen these two surface models with correct genus zero topology in our experiments, but our algorithm can also be applied to high-genus surfaces.

In the rest of this section, we first present experimental results to illustrate the impact of parameters in our algorithm on the generated skeletons. The accuracy of using skeletons to represent cortical folding patterns is validated by comparing manually labeled major sulci to the skeleton of the sulcal regions on 20 cortical surfaces. To illustrate that our algorithm can be applied to general regions on triangulated surfaces, we construct the graphical representations of gyral regions in section IV-C. After that, experimental results on two cortical surfaces generated by BrainVISA are presented.

### A. Parameter selection

There are three parameters in our method that affect the final skeleton. The regularization parameter  $\lambda$  in the graph-cut algorithm controls the smoothness of the segmentation result. The threshold parameter  $F_{thd}$  in the Hamilton-Jacobi skeletonization algorithm and  $S_0$  in the final pruning process both affect the complexity of the final skeleton. As we illustrated in Fig. 8, important branches of the sulcal pattern could be lost if the parameter  $F_{thd}$  is too small, thus in practice we fix its value as the 25th percentile of all flux measures in the sulcal or gyral regions and use  $S_0$  to control the complexity of the final skeleton. Our experience suggests that this provides a good balance between skeleton complexity and the completeness in representing cortical folding patterns. So overall we use the two parameters  $\lambda$  and  $S_0$  to control the final result.

The parameter  $\lambda$  controls the smoothness of the segmentation globally and it should be chosen carefully to prevent some sulcal regions, especially on the medial aspects, from being eliminated. For cortical surface models generated with the method in [19], we find in our practice selecting  $\lambda = 1.0$  provides very good results in terms of boundary smoothness and capturing shallow sulcal regions. Note that a different value might be more suitable for cortical surface models generated by other tools. In this experiment, we computed the skeleton of the sulcal regions, which we denote as the sulcal skeleton, for two cortical surfaces shown in Fig. 10(a) and (e). With the value of the parameter  $\lambda$  fixed at 1.0, we chose three different values for the pruning threshold as  $S_0 = 10mm, 15mm, \text{ and } 20mm$ . The results of the computed skeletons for the two surfaces are plotted in Fig. 10(b)-(d) and (f)-



(h). For the sulcal skeleton of both cortical surfaces, a circular path is plotted in green to illustrate the homotopy-preserving property of the skeleton.

To measure the complexity of the sulcal skeletons, we calculated both the number of branches and connected components in the skeletons. The results are listed below each skeleton in Fig. 10(b)-(d) and (f)-(h). With the increase of  $S_0$ , we can see both measures decrease steadily. This quantifies the visualized reduction of complexity that we observe with the increase of  $S_0$ . For the purpose of analyzing cortex folding patterns, it is important to point out that the selection of the pruning threshold  $S_0$  should depend on the context of the application. For the analysis of neuroanatomy, a relatively smaller  $S_0$  might be useful to have a more complete representation of anatomical structures. On the other hand, we may choose a relatively larger  $S_0$  to generate a compact representation of the sulcal regions for the detection of major sulci.

## B. Validation with manually labeled major sulci

We demonstrated in our previous results that skeletons of sulcal regions provide an explicit, graphical representation of cortical morphometry. In this experiment we evaluate quantitatively the validity of using skeletons to represent cortical folding patterns by measuring the distance from manually labeled sulci to sulcal skeletons. The test data used in this experiment are left hemispheric cortical surfaces that were extracted from the 3D MRI images of the 20 control subjects reported in [50]. The sulcal skeletons of the 20 surfaces were computed with the same set of parameters  $\lambda = 1.0$ ,  $S_0 = 15mm$ . For each subject, 12 major sulci were manually labeled, which include the sylvian fissure, central, precentral, postcentral, superior frontal, inferior frontal, intraparietal, and superior temporal sulcus on the lateral surface, and the calcarine, occipital, cingulate, and olfactory sulcus on the medial surface. On the same cortical surface in Fig. 10(a), we plot the 12 major sulci in Fig. 11(a) and (b) as an illustration. These major sulcal lines were traced manually on the cortical surfaces. Each sulcal line was discretized into 100 evenly spaced points. For the same major sulcus on all 20 surfaces, we first computed the minimal distance from each point on the manually traced curve to the sulcal skeleton of the corresponding cortical surface, and then calculated the 50th, 70th, and 90th percentile of these distances to summarize their distribution. The results for all 12 sulci are shown in Table III. We can see that 90% of the points on all major sulci except the superior frontal sulcus have a minimal distance less than 2mm to the sulcal skeleton. Even for the superior frontal sulcus, the 90th percentile is only slightly larger than 2mm. Since some parts of manually labeled major sulci can cross gyral regions, the results in Table III show very good agreement between manually labeled sulcal lines and automatically detected sulcal skeletons. As an example, the sulcal skeletons in Fig. 10(c) are overlaid with the major sulci in Fig. 11(c) and (d). For better visualization of some buried parts of the sulcal skeletons, we have set the transparency of the cortical surface to 0.75.

The results of this experiment first validate the usage of sulcal skeletons to develop semi-automatic tools for the extraction of major sulci. Once the skeleton is computed, only very few mouse clicks are necessary to pick out each sulcus and this can speedup the manual labeling process. More importantly, this experiment demonstrates sulcal skeletons can capture cortical folding patterns represented by major sulci very accurately and provides quantitative justification for us to perform graph-based analysis of cortical morphometry. Besides the geometrical information that has been represented explicitly in the skeletons, the graphical models derived from sulcal skeletons can act as substrates for other features such as depth, size, and orientation [9], [15] so more detailed analysis of cortical morphometry can be performed.

### C. Gyrals skeletons

For algorithms that rely on the detection of end points to extract sulcal lines [37], sharp corners are assumed to exist for the region of interest. One advantage of our skeletonization approach is that it does not have such limitations and can be applied to general regions. In this experiment, we demonstrate this generality by applying it to gyral regions on cortical surfaces.

If we consider the sulcal regions as lakes on the cortical surface, the gyral regions are then the bank that surrounds the lakes, thus they do not have obvious ending parts. For the cortical surface in Fig. 2, the same process of computing the sulcal skeleton is applied to the gyral regions. Using identical parameters  $\lambda = 1.0$  and  $S_0 = 15mm$ , our method successfully extracts the skeleton of the gyral regions, which we denote as the gyral skeleton, as shown in Fig. 12.

Similar to sulcal skeletons, gyral skeletons also can be used as landmarks in cortical mapping. For example, the anterior part of the superior temporal gyrus, as identified by the blue arrow in Fig. 12(a), is represented as a curve and used as one of the six stable landmarks in the construction of population based cortical atlas [18]. The graphical representation of gyral patterns could also be combined with sulcal skeletons to provide a complete characterization of cortical morphometry since gyri are more commonly used than sulci in describing neuroanatomy.

### D. Application to the gray matter/white matter interface

In this experiment, we applied our algorithm to compute the sulcal skeletons of two cortical surfaces representing the interface between the gray matter and white matter. These surface models were generated by the software package BrainVISA [49] and guaranteed to be of genus zero topology. As shown in Fig. 13(a) and (d), they capture the deep sulcal regions very well.

For these two surfaces, we successfully computed their sulcal skeletons by using the same parameters  $\lambda = 2.0$  and  $S_0 = 15mm$ . Compared with previous examples, a larger  $\lambda$  was chosen to introduce more regularization into the segmentation process as the surfaces here are more convoluted. The sulcal skeletons of the surface in Fig. 13(a) are plotted in Fig. 13(c) and (d) from the lateral and medial views, where the sulcal regions are color mapped as black on the surfaces. The end points of each branch are also marked as yellow dots to visualize the graph structure of the skeletons. For better visualization of the buried parts of the skeletons, we have set the transparency of the surface to 0.75 in these plots. Similarly the sulcal skeletons of the surface in Fig. 13(d) are plotted in Fig. 13(e) and (f). For both surfaces, we can see the sulcal skeletons provide very good characterizations of the folding patterns and they demonstrate the generality of our algorithm to different surface models of the cortex.

## V. Conclusion

A novel approach of characterizing cortical geometry is proposed by computing the Hamilton-Jacobi skeletons of the sulcal and gyral regions on triangulated cortical surfaces. By decomposing skeletons into a set of branches, we can build graphical representations of cortical folding patterns. Our method is designed in the context of analyzing the geometric properties of cortical surfaces, but it is also applicable to compute the skeleton of regions on general triangulated surfaces.

In our current work, we are developing a system for the automatic labeling of major sulci based on the method proposed in this paper. Using the skeleton of the sulcal regions on a

cortical surface, our system generates a sample space for each major sulcal line. The automated labeling is then realized via inferencing over these sample spaces with probabilistic models and machine learning techniques, and very promising results have been obtained [51]. Following the work in [9], [15], we are also investigating the approach of inferencing directly over the graphical models of skeleton branches that are constructed as proposed in section III.B. Not only can this help the detection of major sulci, but also holds great potential for providing new, graph-based techniques of studying cortical morphometry.

## Acknowledgments

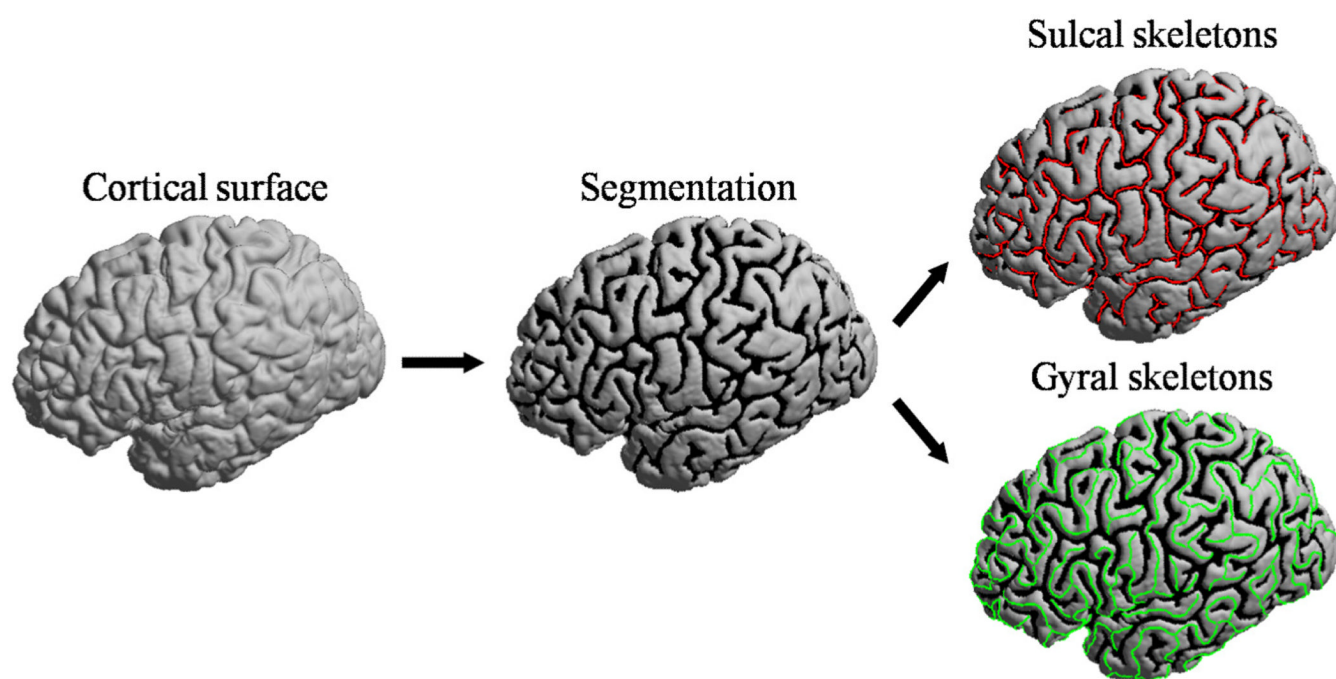
This work was funded by the National Institutes of Health through the NIH Roadmap for Medical Research, Grant U54 RR021813 entitled Center for Computational Biology (CCB). Information on the National Centers for Biomedical Computing can be obtained from <http://nihroadmap.nih.gov/bioinformatics>.

## References

- [1]. Siddiqi K, Bouix S, Tannebaum A, Zucker S. Hamilton-Jacobi skeletons. *Int'l Journal of Computer Vision*. 2002; 48(3):215–231.
- [2]. Welker WI. The significance of foliation and fissuration of cerebellar cortex. the cerebellar folium as a fundamental unit of sensorimotor integration. *Arch. Ital. Biol.* 1990; 128:87–109. [PubMed: 2268185]
- [3]. Ashburner J, Friston KJ. Voxel-based morphometry-the methods. *NeuroImage*. 2000; 11:805–821. [PubMed: 10860804]
- [4]. Toga AW, Thompson PM. Mapping brain asymmetry. *Nature Neurosci. Rev.* 2003; 4(1):37–48.
- [5]. Mangin J-F, Rivière D, Cachia A, Duchesnay E, Cointepas Y, Papadopoulos-Orfanos D, Collins DL, Evans AC, Régis J. Object-based morphometry of the cerebral cortex. *IEEE Trans. Med. Imag.* 2004; 23(8):968–982.
- [6]. Blum H, Nagel R. Shape description using weighted symmetric axis features. *Pattern Recognition*. 1978; 10(3):167–180.
- [7]. Pizer SM, Fritsch DS, Yushkevich PA, Johnson VE, Chaney EL. Segmentation, registration, and measurement of shape variation via image object shape. *IEEE Trans. Med. Imag.* 1999; 18(10): 851–865.
- [8]. Styner M, Gerig G, Joshi S, Pizer S. Automatic and robust computation of 3d medial models incorporating object variability. *Int'l Journal of Computer Vision*. 2003; 55(2/3):107–122.
- [9]. Mangin J-F, Frouin V, Bloch I, Régis J, López-Krahe J. From 3D magnetic resonance images to structural representations of the cortex topography using topology preserving deformations. *Journal of Mathematical Imaging and Vision*. 1995; 5(4):297–318.
- [10]. Lohmann G. Extracting line representations of sulcal and gyral patterns in MR images of the human brain. *IEEE Trans. Med. Imag.* 1998; 17(6):1040–1048.
- [11]. Goualher G, Procyk E, Collins D, Venugopal R, Barillot C, Evans A. Automated extraction and variability analysis of sulcal neuroanatomy. *IEEE Trans. Med. Imag.* 1999; 18(3):206–217.
- [12]. Vaillant M, Davatzikos C. Finding parametric representations of the cortical sulci using an active contour model. *Med. Image. Anal.* 1996; 1(4):295–315. [PubMed: 9873912]
- [13]. Zhou Y, Thompson PM, Toga AW. Extracting and representing the cortical sulci. *IEEE Computer Graphics and Applications*. 1999; 19(3):49–55. [PubMed: 20830215]
- [14]. Zeng, X.; Staib, L.; Schultz, R.; Tagare, H.; Win, L.; Duncan, J. A new approach to 3D sulcal ribbon finding from MR images; *Proc. MICCAI*; 1999; p. 148-157.
- [15]. Rivière D, Mangin J-F, Papadopoulos-Orfanos D, Martinez J, Frouin V, Régis J. Automatic recognition of cortical sulci of the human brain using a congregation of neural networks. *Med. Image. Anal.* 2002; 6:77–92. [PubMed: 12044997]
- [16]. Fischl B, Sereno MI, Tootell RBH, Dale AM. High-resolution intersubject averaging and a coordinate system for the cortical surface. *Human Brain Mapping*. 1999; 8:272–284. [PubMed: 10619420]

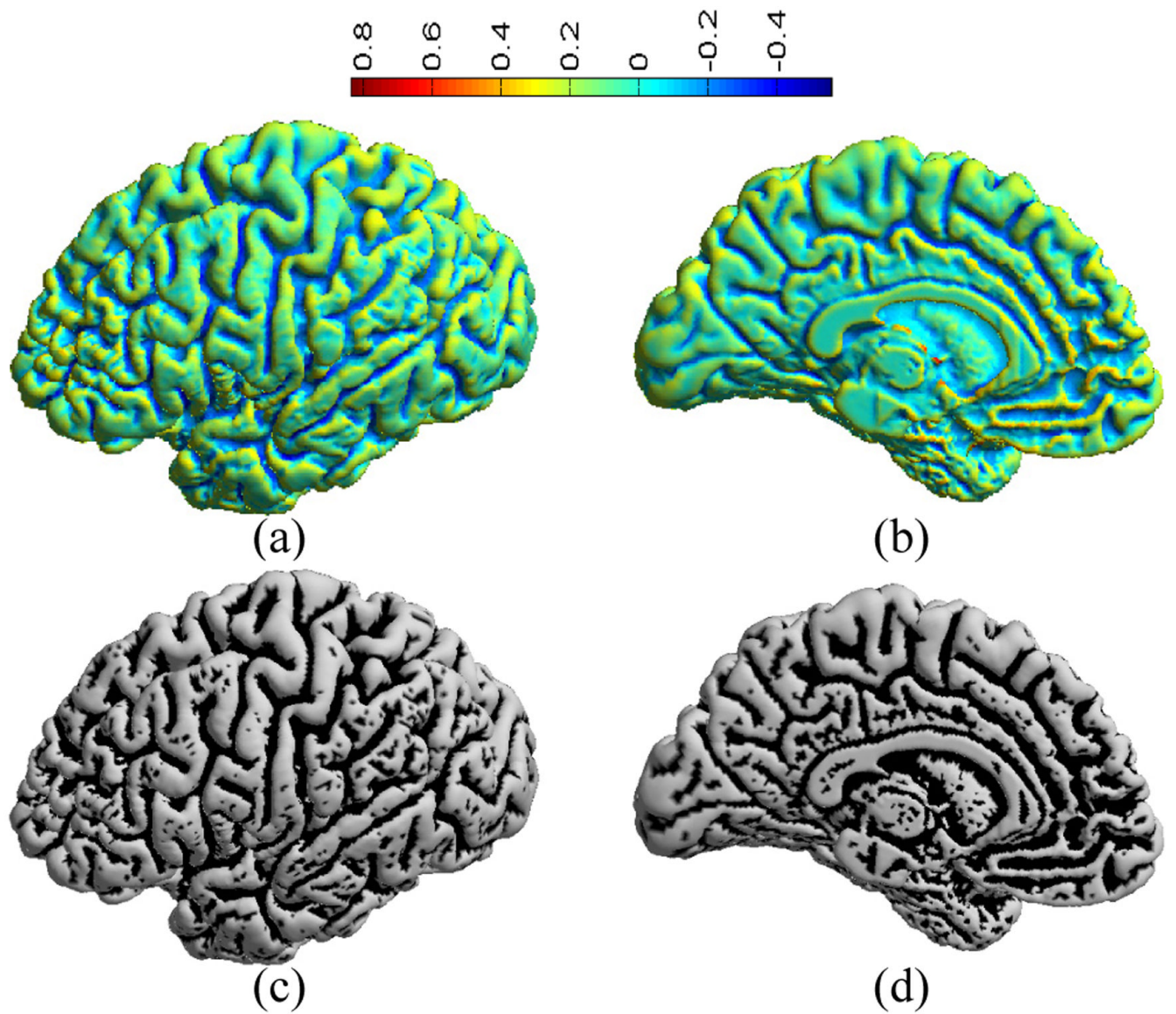
- [17]. Thompson PM, Hayashi KM, Sowell ER, Gogtay N, Giedd JN, Rapoport JL, de Zubicaray GI, Janke AL, Rose SE, Semple J, Doddrell DM, Wang Y, van Erp TGM, Cannon TD, Toga AW. Mapping cortical change in alzheimers disease, brain development, and schizophrenia. *NeuroImage*. 2004; 23:S2–S18. [PubMed: 15501091]
- [18]. Van Essen DC. A population-average, landmark- and surface-based (PALS) atlas of human cerebral cortex. *NeuroImage*. 2005; 28(3):635–62. [PubMed: 16172003]
- [19]. MacDonald, D. Ph.D. dissertation. McGill Univ.; Canada: 1998. A method for identifying geometrically simple surfaces from three dimensional images.
- [20]. Dale AM, Fischl B, Sereno MI. Cortical surface-based analysis i: segmentation and surface reconstruction. *NeuroImage*. 1999; 9:179–194. [PubMed: 9931268]
- [21]. Fischl B, Sereno MI, Dale AM. Cortical surface-based analysis ii: Inflation, flattening, and a surface-based coordinate system. *NeuroImage*. 1999; 9(2):195–207. [PubMed: 9931269]
- [22]. Cointepas Y, Mangin J-F, Garnero L, Poline J, Benali H. BrainVISA: Software platform for visualization and analysis of multi-modality brain data. *NeuroImage*. 2001; 13(6):S98.
- [23]. Shattuck D, Leahy R. BrainSuite: An automated cortical surface identification tool. *Med. Image. Anal.* 2002; 8(2):129–142. [PubMed: 12045000]
- [24]. Han X, Pham DL, Tosun D, Rettmann ME, Xu C, Prince J. CRUISE: Cortical reconstruction using implicit surface evolution. *NeuroImage*. 2004; 23:997–1012. [PubMed: 15528100]
- [25]. Kim JS, Singh V, Lee JK, Lerch J, Ad-Dab'bagh Y, MacDonald D, Lee JM, Kim SI, Evans AC. Automated 3-d extraction and evaluation of the inner and outer cortical surfaces using a laplacian map and partial volume effect classification. *NeuroImage*. 2005; 27:210–221. [PubMed: 15896981]
- [26]. Xu M, Thompson PM, Toga AW. Adaptive reproducing kernel particle method for extraction of the cortical surface. *IEEE Trans. Med. Imag.* 2006; 25(6):755–767.
- [27]. Bertrand G, Mourgouyres R. Some topological properties of surfaces in  $\mathbb{Z}^3$ . *J. Math. Imaging. Vis.* 1999; 11:207–221.
- [28]. Han X, Xu C, Prince J. A topology preserving level set method for geometric deformable models. *IEEE Trans. Pattern Anal. Machine Intell.* Jun; 2003 25(6):755–768.
- [29]. Ono, M.; Kubik, S.; Abarnathey, C. *Atlas of the Cerebral Sulci*. Thieme Medical Publishers; 1990.
- [30]. Shi Y, Thompson PM, Dinov I, Osher S, Toga AW. Direct cortical mapping via solving partial differential equations on implicit surfaces. *Med. Image. Anal.* 2007; 11(3):207–223. [PubMed: 17379568]
- [31]. Khaneja N, Miller M, Grenander U. Dynamic programming generation of curves on brain surfaces. *IEEE Trans. Pattern Anal. Machine Intell.* 1998; 20(11):1260–1265.
- [32]. Bartesaghi A, Sapiro G. A system for the generation of curves on 3D brain images. *Human Brain Mapping*. 2001; 14:1–15. [PubMed: 11500986]
- [33]. Tao X, Prince J, Davatzikos C. Using a statistical shape model to extract sulcal curves on the outer cortex of the human brain. *IEEE Trans. Med. Imag.* 2002; 21(5):513–524.
- [34]. Mémoli F, Sapiro G, Thompson PM. Implicit brain imaging. *Neuroimage*. 2004; 23(Suppl 1):S179–S188. [PubMed: 15501087]
- [35]. Lui, LM.; Wang, Y.; Chan, TF.; Thompson, PM. Automatic landmark and its application to the optimization of brain conformal mapping; *Proc. CVPR*; 2006; p. 1784-1792.
- [36]. Tu Z, Zheng S, Yuille A, Reiss A, Dutton RA, Lee A, Galaburda A, Dinov I, Thompson P, Toga A. Automated extraction of the cortical sulci based on a supervised learning approach. *IEEE Trans. Med. Imag.* 2007; 26:541–552.
- [37]. Kao C, Hofer M, Sapiro G, Stern J, Rehm K, Rotterberg D. A geometric method for automatic extraction of sulcal fundi. *IEEE Trans. Med. Imag.* 2007; 26(4):530–540.
- [38]. Rettmann ME, Han X, Xu C, Prince JL. Automated sulcal segmentation using watersheds on the cortical surface. *NeuroImage*. 2002; 15(2):329–244. [PubMed: 11798269]
- [39]. Rex DE, Ma JQ, Toga AW. The LONI Pipeline processing environment. *NeuroImage*. 2003; 19(3):1033–1048. [Online]. Available: <http://www.loni.ucla.edu/pipeline>. [PubMed: 12880830]

- [40]. Osher S, Sethian J. Fronts propagation with curvature-dependent speed: algorithms based on Hamilton-Jacobi formulations. *Journal of computational physics*. 1988; 79(1):12–49.
- [41]. Cachia A, Mangin J-F, Riviere D, Kherif F, Boddaert N, Andrade A, Papadopoulos-Orfanos D, Poline J-B, Bloch I, Zilbovicius M, Sonigo P, Brunelle F, Régis J. A primal sketch of the cortex mean curvature: a morphogenesis based approach to study the variability of the folding patterns. *IEEE Trans. Med. Imag.* 2003; 22(6):754–765.
- [42]. Geman S, Geman D. Stochastic relaxation, gibbs distributions, and the bayesian restoration of images. *IEEE Trans. Pattern Anal. Machine Intell.* 1984; 6(6):721–741.
- [43]. Besag J. On the statistical analysis of dirty pictures. *J. R. Statist. Soc. B.* 1986; 48(3):259–302.
- [44]. Boykov, Y.; Jolly, MP. Interactive graph cuts for optimal boundary & region segmentation of objects in N-D images; *Proc. ICCV*; 2001; p. 105-112.
- [45]. Boykov Y, Kolmogorov V. An experimental comparison of Min-Cut/Max-Flow algorithms for energy minimization in vision. *IEEE Trans. Pattern Anal. Machine Intell.* Sep; 2004 26(9):1124–1137.
- [46]. Kimmel R, Sethian JA. Computing geodesic paths on manifolds. *Proc. Natl. Acad. Sci. USA.* 1998; 95(15):8431–8435. [PubMed: 9671694]
- [47]. Kong T, Rosenfeld A. Digital topology: introduction and survey. *Comput. Vis. Graph. Image Process.* Dec; 1989 48(3):357–393.
- [48]. Cachia A, Mangin J-F, Riviere D, Papadopoulos-Orfanos D, Kherif F, Bloch I, Régis J. A generic framework for the parcellation of the cortical surface into gyri using geodesic vorono diagrams. *Med. Image. Anal.* 2003; 7(4):403–416. [PubMed: 14561546]
- [49]. Cointepas Y, Mangin J-F, Garnero L, Poline J-B, Benali H. BrainVISA: Software platform for visualization and analysis of multi-modality brain data. *NeuroImage*. 2001; 13(6, Supplement 1): 98.
- [50]. Lin J, Salamon N, Lee A, Dutton R, Geaga J, Hayashi K, Luders E, Toga A, Thompson P. Reduced neocortical thickness and complexity mapped in mesial temporal lobe epilepsy with hippocampal sclerosis. *Cereb. Cortex*. Nov.2006 J. E. Jr. doi: doi:10.1093/cercor/bhl109.
- [51]. Shi, Y.; Tu, Z.; Reiss, A.; Dutton, R.; Lee, AD.; Galaburda, A.; Dinov, I.; Thompson, PM.; Toga, AW. Joint sulci detection using graphical models and boosted priors; *Proc. IPMI*; 2007; p. 98-109.

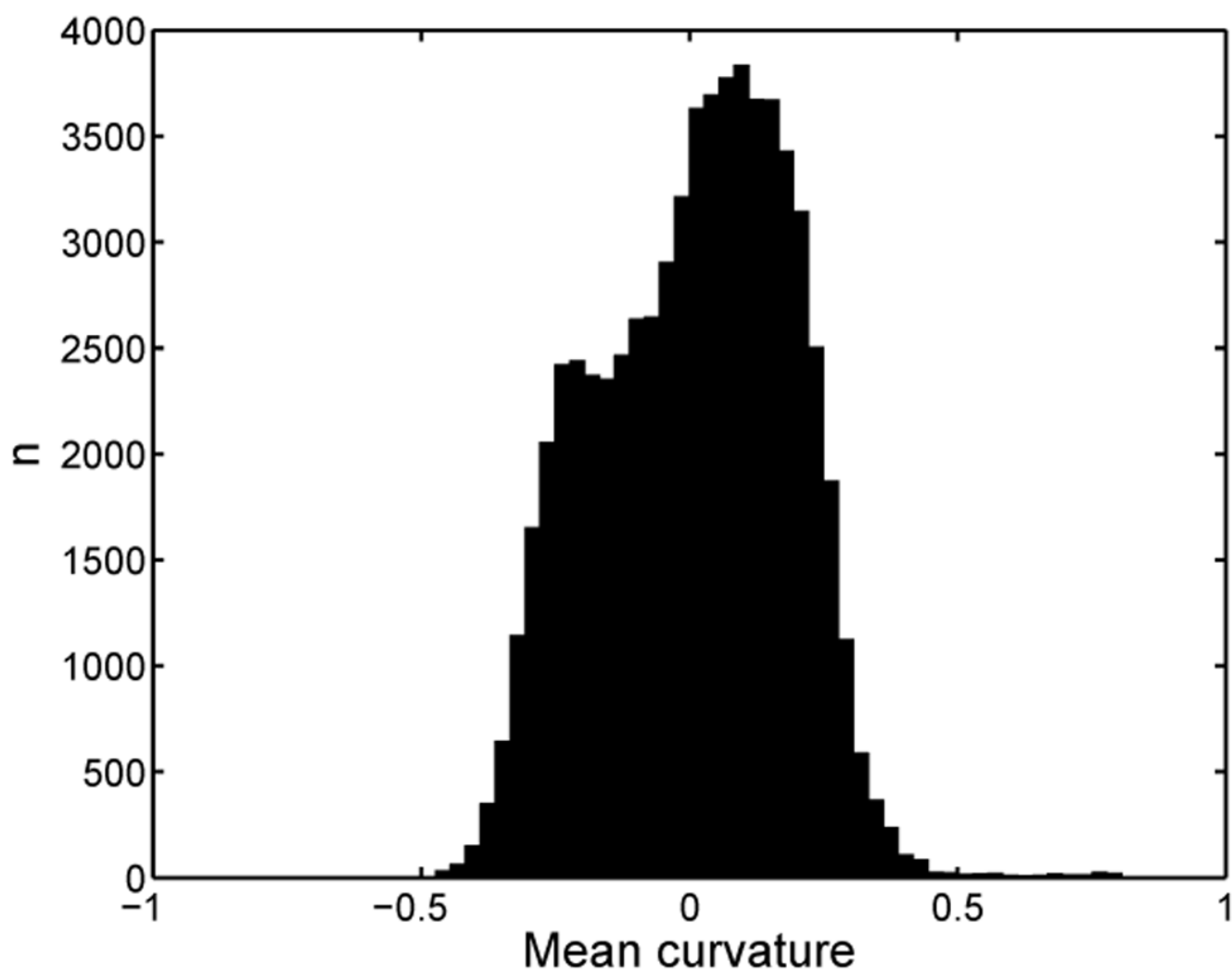


**Fig. 1.**  
The main steps in our algorithm.

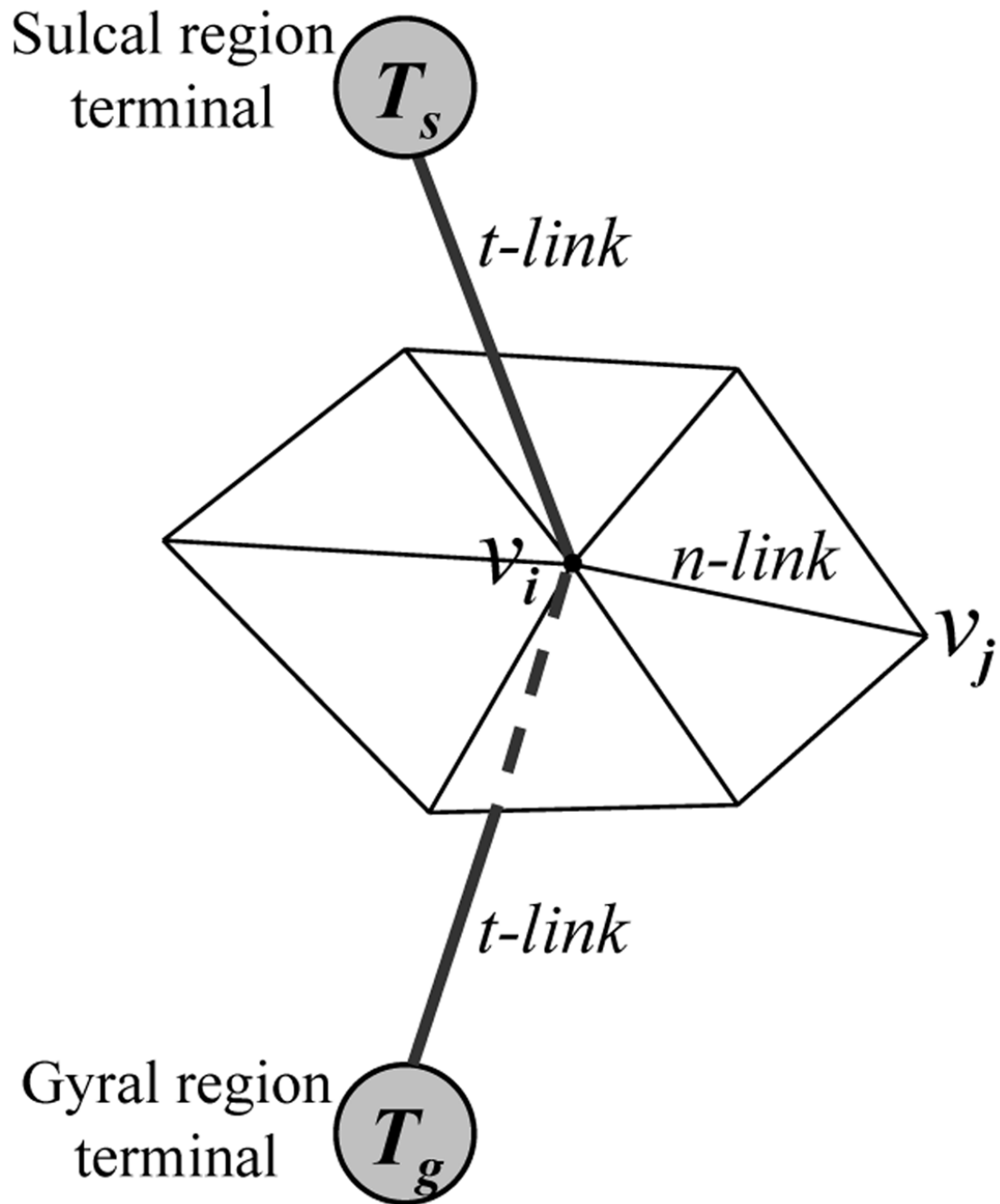




**Fig. 2.** The mean curvature of a cortical surface(a)(b) and the segmentation result obtained by thresholding according to the sign of the mean curvature(c)(d). (a)(c) Lateral view. (b)(d) Medial view.

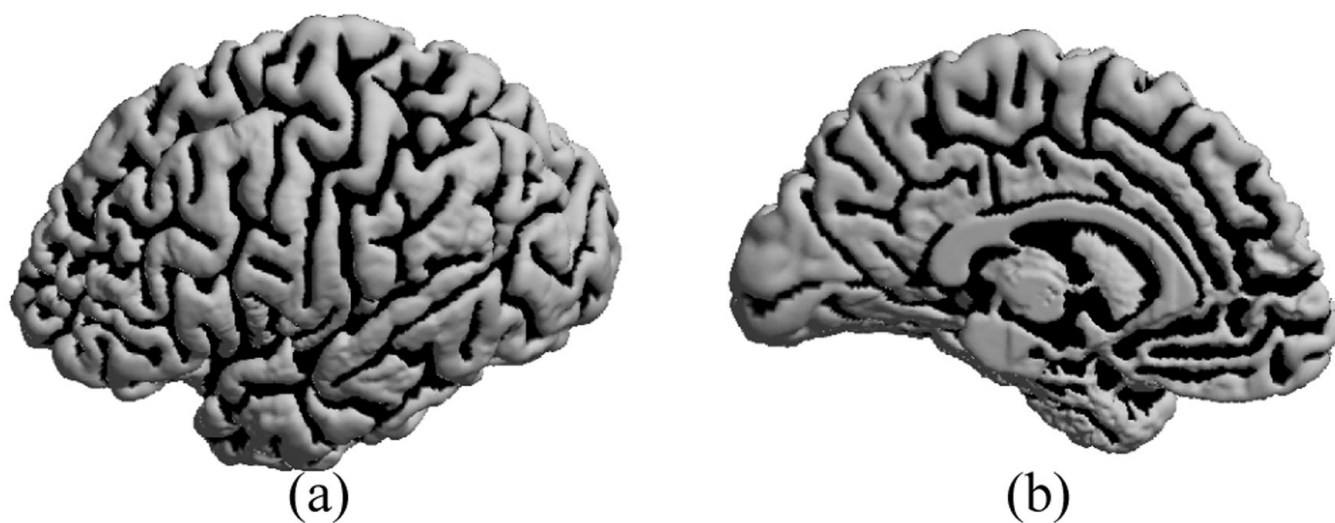


**Fig. 3.**  
The histogram of the mean curvature distribution on the cortical surface shown in Fig. 2 (a) and (b)

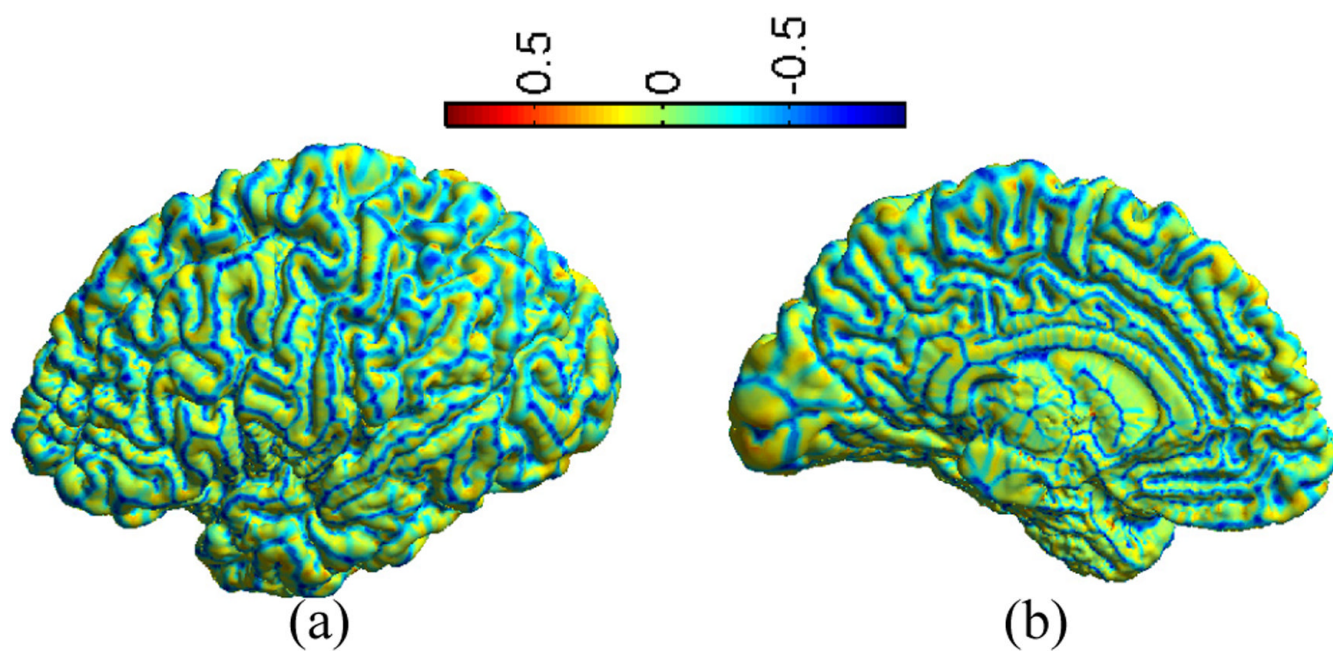


**Fig. 4.**

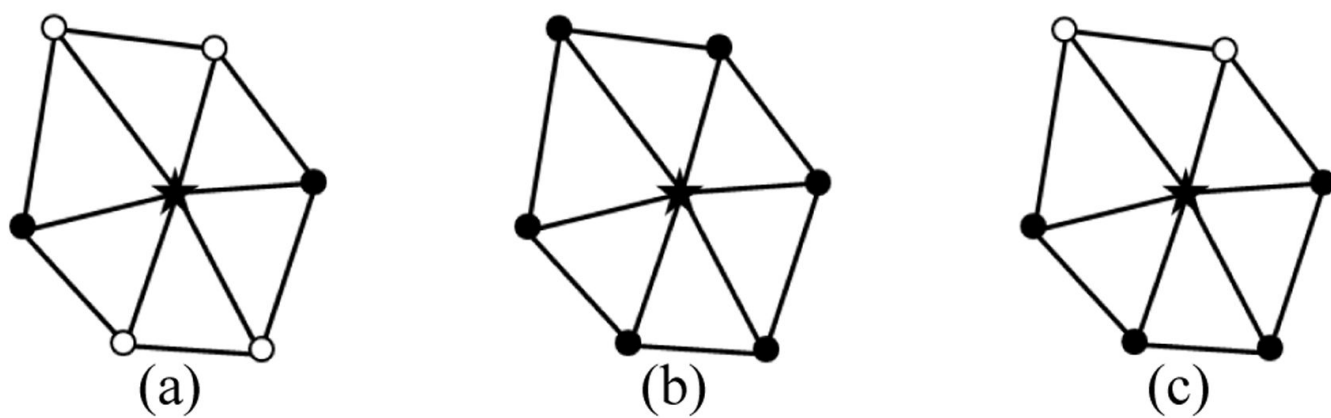
Graph construction for the minimization of the variational energy.



**Fig. 5.**  
Graph-cut segmentation results. (a) Lateral view. (b) Medial view.

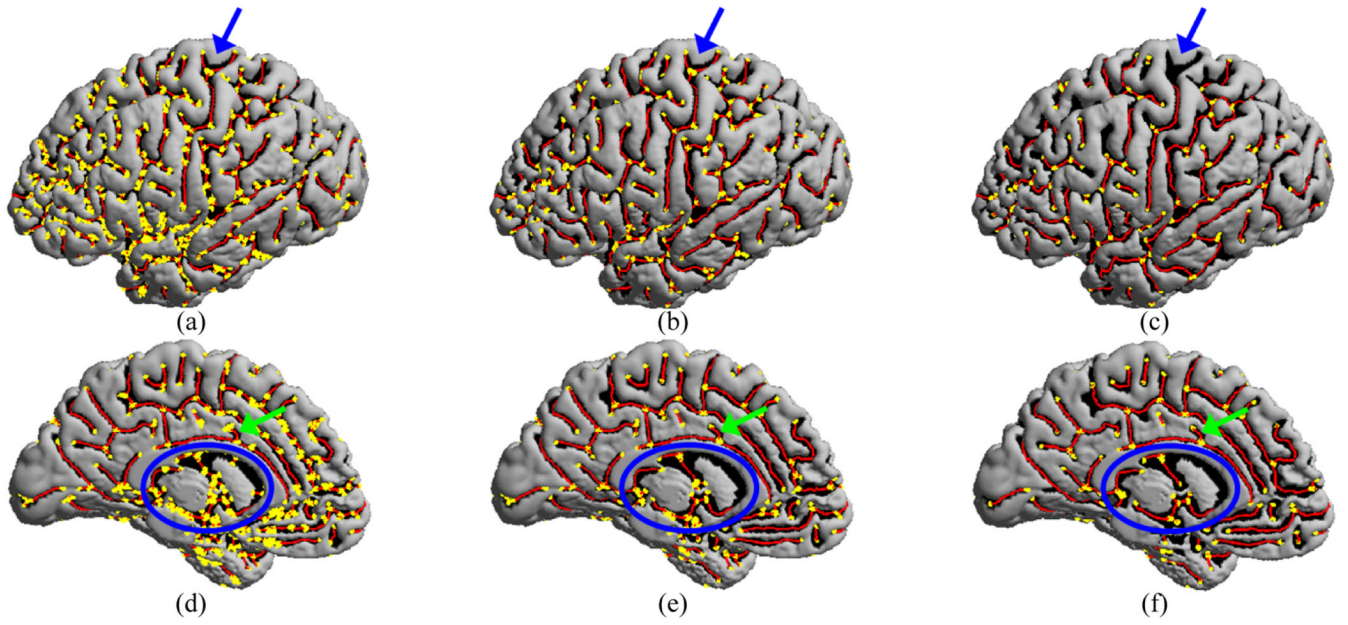


**Fig. 6.**  
The flux measure for each vertex of the cortical surface. (a) Lateral view. (b) Medial view.

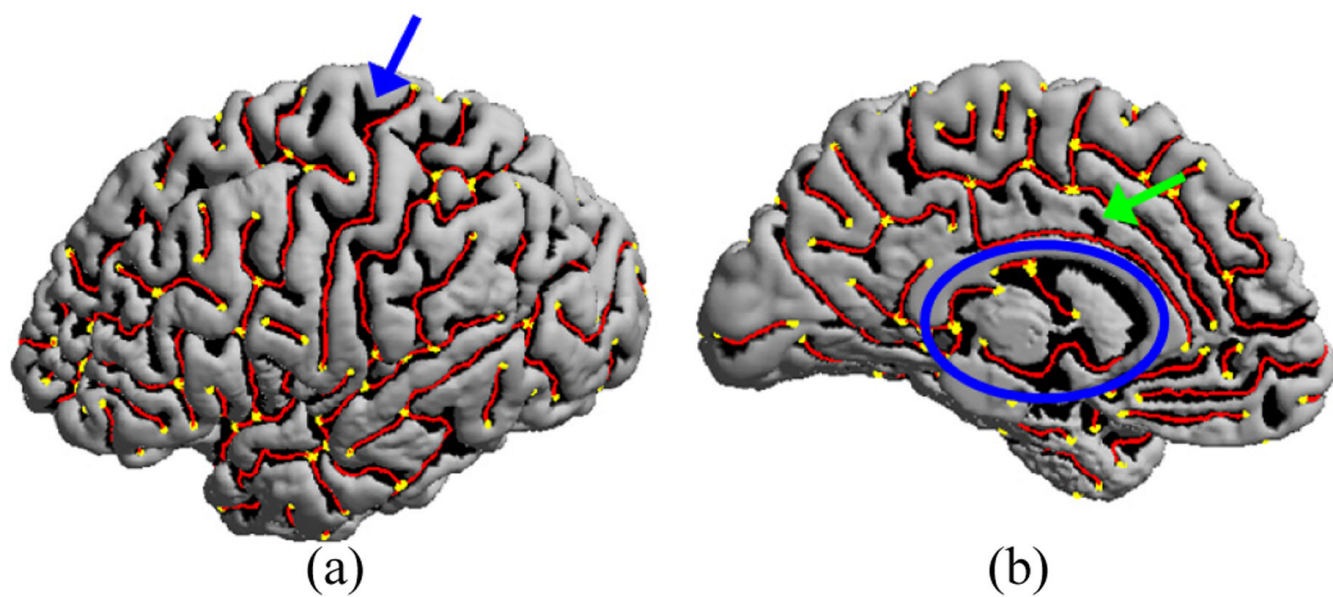


**Fig. 7.** Three cases of the 1-ring neighborhood of the vertex represented as \*, where ● and ○ are vertices in the object and background region, respectively.

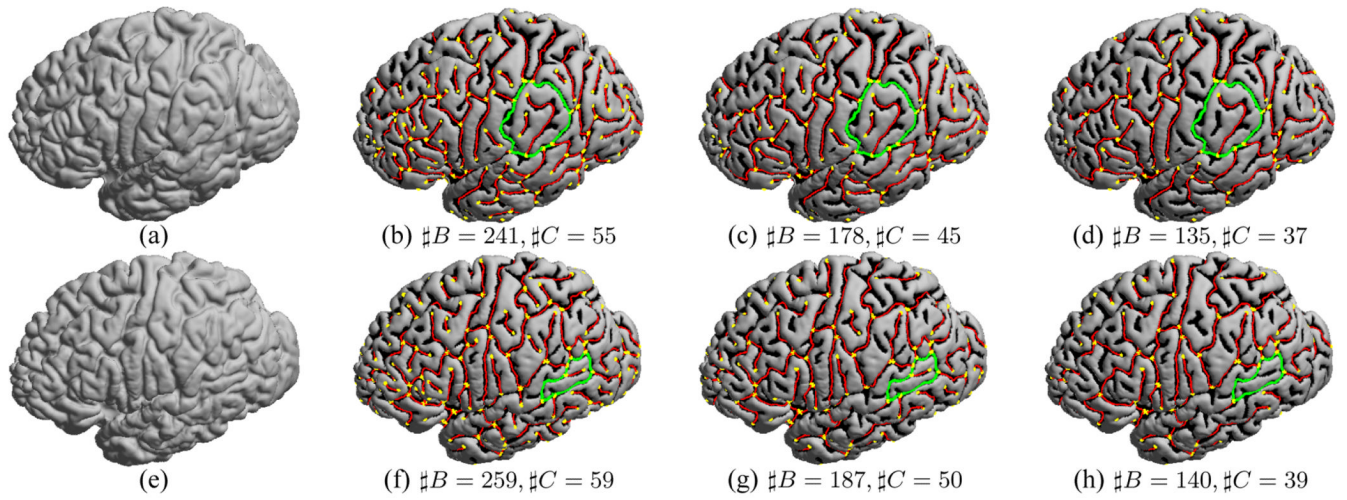




**Fig. 8.** The Hamilton-Jacobi skeleton obtained by choosing the threshold  $F_{thd}$  at the 50th percentile(a)(d); 25th percentile(b)(e); and 5th percentile(c)(f) of the flux measures from all vertices in the sulcal regions.



**Fig. 9.**  
The pruned skeleton. (a) Lateral view. (b) Medial view.

**Fig. 10.**

Sulcal skeletons of two cortical surfaces obtained by choosing  $\lambda = 1.0$  and three different values for the pruning threshold  $S_0$ . (a)(e) Cortical surfaces. (b)(f)  $S_0 = 10mm$ . (c)(g)  $S_0 = 15mm$ . (d)(h)  $S_0 = 20mm$ . For each surface, a circular path is highlighted in green. The number of branches( $\#B$ ) and connected components( $\#C$ ) are listed below the skeletons.

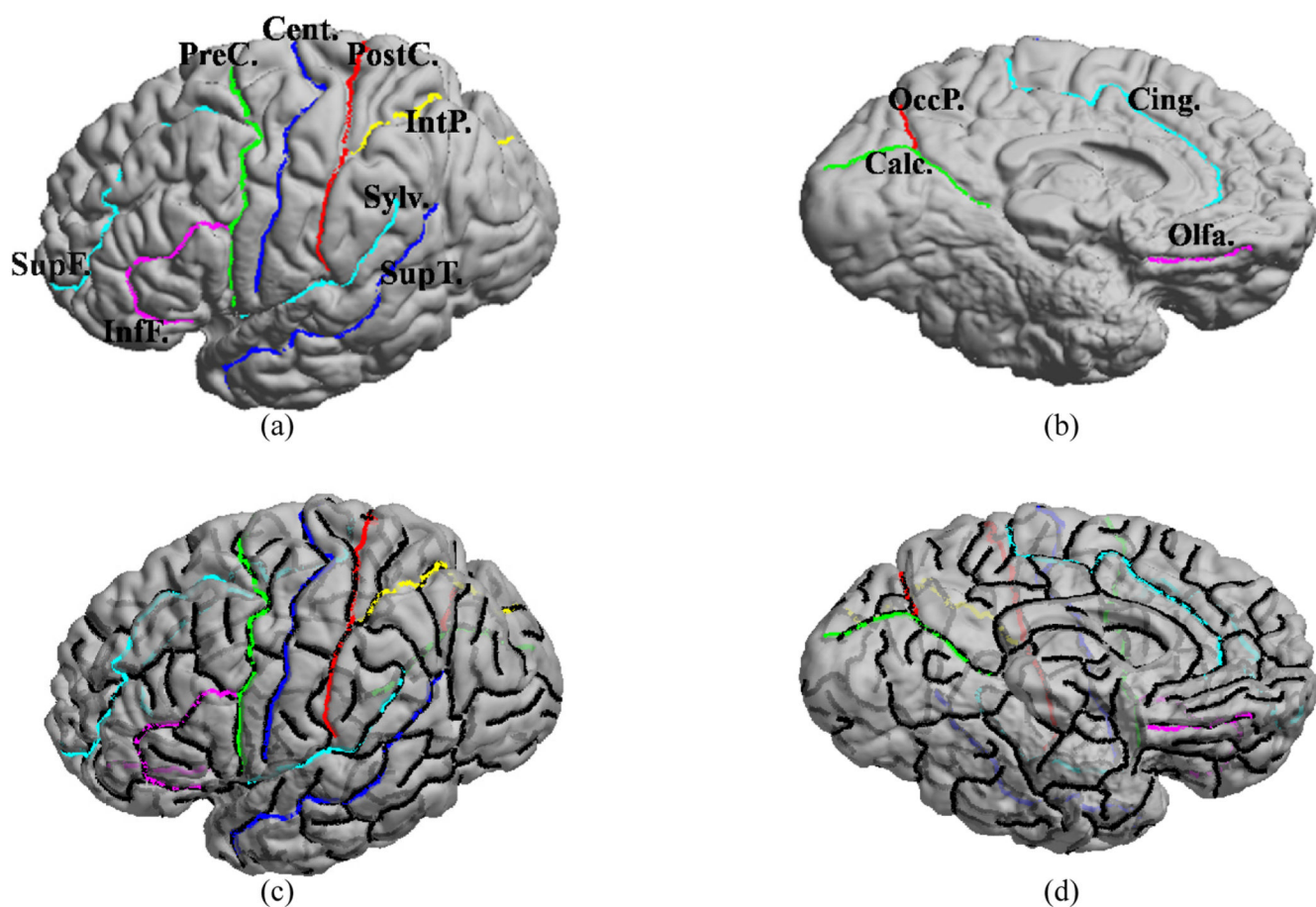


**Fig. 11.**

An illustration of the 12 major sulci used in our experiment. (a)(c) Lateral side. (b)(d) Medial side. The major sulci are overlaid with sulcal skeletons in (c) and (d), where the sulcal skeletons are plotted as black lines.



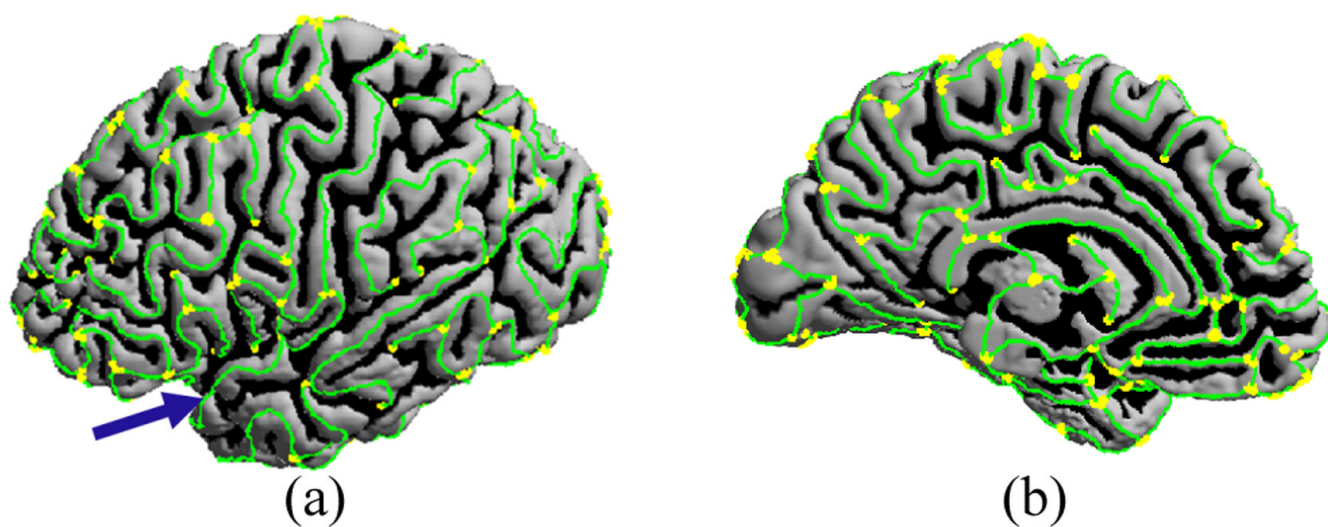


**Fig. 12.** Visualization of the gyral skeleton, where terminal points of each branch are marked as yellow dots. (a) Lateral view. (b) Medial view.

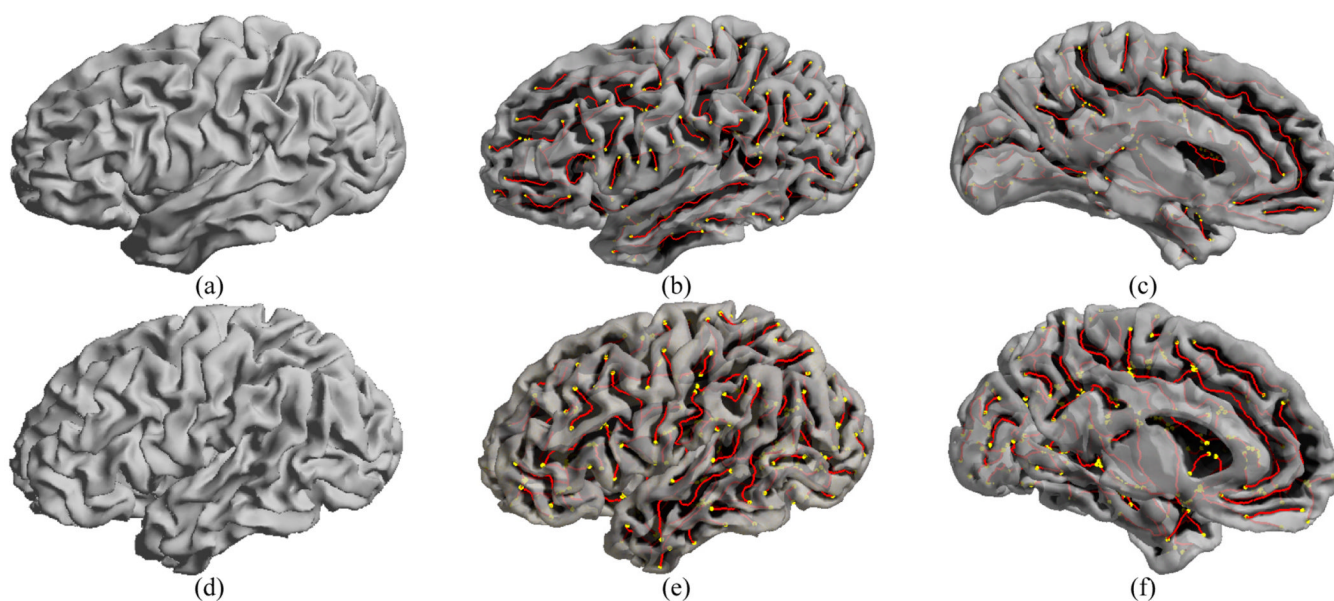


**Fig. 13.** Sulcal skeletons of two surfaces generated with BrainVISA. (a)(d) Surfaces. (b)(e) Lateral view. (c)(f) Medial view.



**TABLE I**

The algorithm to compute the Hamilton-Jacobi skeleton of a subset  $\mathcal{O}$  on  $\mathcal{M}$

---

```

Compute the geodesic distance transform  $D$  of  $\mathcal{O}$  on  $\mathcal{M}$ .
Compute the flux measure at each vertex in  $\mathcal{O}$  using Eq. (5).
Initialize a heap  $\mathbf{H}$  with vertices on the boundary of  $\mathcal{O}$  using the flux measure as the sorting key.
do
     $P = \text{PopHeap}(\mathbf{H})$ .
    if  $P$  is a simple point
        if  $P$  is not an end point or  $\text{Flux}(P) > F_{thd}$ 
            Remove  $P$  from  $\mathcal{O}$ .
            Insert neighbors of  $P$  to  $\mathbf{H}$  if they are simple points.
        else
            Mark  $P$  as a skeletal point.
    end
end
while( $\mathbf{H}$  is not empty)

```

---

**TABLE II****The Skeleton Pruning Algorithm**


---

<b>1</b>	Compute the pruning weight for all branches in $B_I \cup B_T$ .
<b>2</b>	Find the branch $\hat{b}$ in $B_I \cup B_T$ with the smallest weight. If the weight is larger than $S_0$ , stop the pruning process; otherwise, eliminate this branch from the skeleton.
<b>3</b>	If $\hat{b}$ has two neighbors, merge them into one branch.
<b>4</b>	Update the neighboring relation, branch type, and pruning weight of branches connected with $\hat{b}$ . Return to step 2.

---

Quantile statistics for the distribution of the minimal distances from manually traced major sulci to sulcal skeletons. The unit of the distance is millimeter

TABLE III

	Cent.	PreC.	PostC.	SupF.	InfF.	IntP.	Sylv.	SupT.	Calc.	OccP.	Cing.	Olf.
50th percentile	0.47	0.51	0.61	0.62	0.48	0.65	0.42	0.40	0.36	0.22	0.22	0.78
70th percentile	0.71	0.85	0.98	1.05	0.85	0.97	0.69	0.63	0.51	0.32	0.31	1.22
90th percentile	1.27	1.71	1.83	2.13	1.80	1.73	1.28	1.29	0.93	0.56	0.54	1.92